# Investigation of diffusive and optical properties of vapour-air mixtures: The benefits of interferometry

V. Shevchenko[a], A. Mialdun[b], V. Yasnou[b], Y. V. Lyulin[a], H. Ouerdane[a], V. Shevtsova[c,d]

[a] *Center for Energy Science and Technology, Skolkovo Institute of Science and Technology, 3 Nobel Street, 121205 Moscow, Russia*
[b] *Microgravity Research Centre, CP-165/62, Université libre de Bruxelles (ULB), av. F. D. Roosevelt 50, B-1050, Brussels, Belgium*
[c] *Basque Foundation for Science, Bilbao, Spain*
[d] *Mechanical and Manufacturing Department, Mondragon Goi Eskola Politeknikoa (MGEP), Loramendi 4, Apdo. 23, 20500 Mondragon, Spain*

## Abstract

While interferometry has been widely used for diffusion measurements in liquid mixtures, it was hardly applied so far to vapour-gas mixtures. The present work aims to bridge this gap. Using an improved Mach-Zehnder interferometer, we investigate the evaporation of acetone and HFE-7100 in ambient air. Our observations build on complete evaporation of a thin liquid layer in a cell with open end, at ambient temperature varying between 283.15 and 313.15 K. Monitoring the evolution of the refractive index change allows us to determine the evaporation rate and vapour-in-air diffusion coefficients. The spatial distribution of the refractive index reveals that the purely diffusive mode of transport is perturbed at both ends of the cell. Interferometric images facilitate isolating these regions, determining the true diffusion path, and hence, the correct diffusion coefficients. Besides, we illustrate the possibility of calculating the optical contrast factors, which we find in excellent agreement with current experiments.

*Keywords:* Interferometry, Vapor-in-air diffusion coefficient, Vapor optical properties, acetone, HFE-7100

## 1. Introduction

Evaporation from free liquid surfaces is a heat transfer mode that plays a crucial role in chemical engineering, biology, and practical applications such as, e.g., humidification of air, spray cooling, drying, and delivery of medical aerosols to name a few. The actual needs for the experimental assessment of the gases diffusive properties thus range from very practical purposes such as defense – diffusion of warfare gases or their simulants in air [1], to purely academic ones, e.g. an experimental support of the Chapman-Enskog theory [2]. It is also worth noting that in the electronic industry, the current intensive development of efficient cooling systems and heat pumps based on liquid–vapor–liquid phase transitions [3, 4] triggers a renewed interest for the diffusive properties of vapour-gas mixtures, as vapor transport through a gas phase appears to be a limiting factor.

Diffusion in a given system is the slow transport of matter, spreading from one region to another, caused by concentration gradients. It is a complex process that depends also on the thermodynamic conditions, notably pressure and temperature, and chemical concentration and phase of the environment where it occurs. The diffusion coefficient of vapor in gas is one of the important parameters used in mathematical modelling and numerical simulations of heat and mass transfer through the gas-liquid interfaces [5, 6, 7]. To predict precisely the global evaporation rate from the liquid surface into gas, one may use the values of the diffusion coefficients given in benchmark databases [8]. However, the determination of the global evaporation rate averaged over a certain time period and measured in many experiments is not enough to understand well all fundamental aspects in the evaporation process from the free surface.

Non-uniform evaporation from gas-liquid interfaces, which takes place in most actual evaporative systems, can change flow patterns within a liquid volume. For instance, the Marangoni effect due to a non-uniform evaporation providing thermocapillary stresses on the liquid surface is a reason of the complex convection in liquid layers [9]. In some cases the thermocapillary effects may

cause the breakdown of liquid film [10]. It is evident that the cross-influence study of convection and evaporation should be considered in terms of the local evaporation rate from the gas-liquid interfaces. The determination of the local evaporation rates bears a particular importance in the study of heat and mass transfer in the contact line zone of the liquid droplets [11]. Considering more specifically the evaporation from surfaces of liquid droplets [12, 13, 14], bridges [15] and layers [16, 17], either in a stationary or moving gaseous environment, the evaporation rate is limited by the vapor diffusion into the gas. Fick's laws for steady-state and time-dependent regimes, are widely used to determine the evaporation rate from gas-liquid interface into gas phase, for which the knowledge of the diffusion coefficients as function of the vapor temperature is needed. However, lack of systematic measured data of their diffusive and optical properties as functions of temperature in gases, in the benchmark databases, hinders progress.

Diffusion coefficients can be obtained by various experimental methods such as, e.g., Laser induced fluorescence (PLIF) [18] or Fourier transform infrared spectrometry (FTIR) [19]. These optical techniques can be used for measuring local evaporation rates or vapor concentrations over gas-liquid interfaces, but they do not show sufficient resolution for the analysis of vapour concentration gradients in the gas phase. Measurement of the vapor concentration and local evaporation rate require the knowledge of the vapor-gas mixture refractive index variation with vapor concentration, i.e. the so-called optical contrast factor. Interferometry is another optical measurement technique, which is sensitive enough to quantify the amount of vapor in gas [20, 21, 22], and hence which is well-suited for our purpose. In fact, application of digital interferometry was found to be an optimal solution for measuring the local distribution of the evaporation rate along the liquid surface from a direct measurement of the vapour concentration gradient normal to the gas-liquid interface [22]; and it is particularly successful for substances featuring high molar mass and significant partial vapor pressure. In addition, optical digital interferometry is widely and successfully used for measuring diffusion and thermal diffusion coefficients in

3

liquid mixtures [23, 24, 25]

Despite a number of new and competing techniques to measure the binary gas diffusivities, the Stefan tube method, introduced in the end of 19th century, is still very popular due to its simplistic arrangement. An overview of the method can be found in [26], where condensed but detail-reach description of the technique is supplemented with a deep analysis of possible error sources. Some practical problems have been discussed already in [26], and extensively studied later on [27, 28, 29, 30]. Nevertheless, the method is in continuous use, and even is modified to cover wider use-cases, e.g. when the data is needed at temperatures exceeding boiling point [31], although, the use of non-volatile solvent may also introduce a bias in the result [32]. The first attempts to apply interferometry to the Stefan tube date back to the 1960s [20, 21], with the data treatment being limited at the time to manual fringe tracking method.

When using an evaporation-diffusion tube for measuring diffusion coefficients, experiments rely on the monitoring the rate of evaporating liquid loss, either by visual tracking of the liquid level [27, 32], or, gravimetrically [33, 34]. In the present study, even if a somewhat similar geometry is used, the observation is built on the complete evaporation of a thin liquid layer placed in a cell with open end designed for optical measurements.

Two often-used liquids with a very different volatility were selected for tests: HFE-7100 and acetone. HFE-7100 is a low volatile liquid, and since it has low surface tension and low viscosity, it penetrates into tight spaces in delicate electronic equipment, which makes it suitable for thorough and complete cleaning. HFE-7100 is also widely used as heat-transfer liquid in electronics. Acetone, on the other hand, is a highly volatile liquid that is well characterised and therefore suitable for validating the experimental approach.

In the present study, Mach-Zehnder interferometry with improved stability combined with modern digital interferogram processing based on 2D Fourier transform, is applied to measure the diffusion coefficient and optical properties of selected vapors in air. Considering HFE-7100 and acetone, we present and discuss the evaporation rates, refractive indices and optical contrast factors, as

4

well as vapor diffusion coefficients in air. The temperature dependence of the measured quantities is investigated over a 30 K range, starting from 283.15 K.

The goal of the article is two-fold: on the one hand, to demonstrate the value of digital interferometry for the measurement of the diffusive and optical properties of vapour-air mixtures and, on the other hand, to provide precise measurement data of these properties for acetone and HFE-7100 vapours in air. The article is organized as follows. In Section 2, we describe the experimental setup and procedure, with a focus on the optical technique. The experimental results are presented and discussed in Section 3. Concluding remarks are given in Section 4. Additional data and technical details are given in the accompanying Supplemental Information.

## 2. Experimental

### 2.1. Materials

Two liquids were used in the experiments: acetone of the purity $\geq 99.8\%$ (for analysis, EMSURE® ACS, ISO, Reag. Ph Eur), supplied by Merck, and HFE-7100 (Novec™ 7100 Engineered Fluid), of the purity $\geq 99.5\%$, purchased from Sigma-Aldrich. Both liquids were used without further purification. The main characteristics of the liquids are listed in Table 1.

### 2.2. Interferometer

In the present work, a Mach-Zehnder interferometer is used to measure the vapor concentration inside the rectangular cell. The experimental setup, consisting of the optical cell, interferometer, video acquisition and thermostabilizing systems, is depicted in Fig. 1. A coherent light beam is generated by a red diode-pumped solid-state laser RLTMRL-671 of Roithner LaserTechnik (wavelength $\lambda = 671$ nm, $\text{TEM}_{00}$ beam profile, and output power ranging from 1 to 200 mW). The beam is expanded by a spatial filter, then passes through a collimating lens and at the exit its diameter covers the entire area of the cell. Then, the beam splitter (BS1) divides the beam into two parts of equal intensity

Table 1: Properties of the liquids used in the experiments on evaporation. All the properties are given for the reference temperature of 298.15 K.

|  | Acetone | HFE-7100 |
| --- | --- | --- |
| Chemical name | Propan-2-one | Methoxy-nonafluorobutane |
| CAS No. | 67-64-1 | 163702-08-7, 163702-07-6 |
| Chemical formula | $C_3H_6O$ | $C_4F_9OCH_3$ |
| Molar mass $M$, $g\,mol^{-1}$ | 58.08 | 250 |
| Density $\rho$, $kg\,m^{-3}$ | 784.24 | 1481.57 |
| Thermal expansion $\beta_T$, $10^{-3}$ $K^{-1}$ | 1.56 | 1.53 |
| Thermal conductivity $k$, $W\,m^{-1}\,K^{-1}$ | 0.159 | 0.068 |

(reference and objective). The objective beam traverses the experimental cell while the reference beam bypasses the cell in the open air. Changes in both temperature and concentration due to phase change in the cell contribute to the spatial distribution of the refractive index in the objective beam. Then, the two beams are redirected by mirrors M1 and M2 to spatially join at the second beam splitter (BS2). The appropriate tilting angle and width of interference fringes can be adjusted by varying the inclination angle of the mirrors M1, M2. Large aperture optics was used for monitoring a cell height up to 45-48 mm: 2" diameter mirrors and beam splitters. The resulting interference pattern is captured by the CCD camera of JAI CV-M4+CL with the resolution of $1280 \times 1024$ pixels and frame rate up to 24 fps. A Thorlabs MVL50HS lens (focal length 50 mm and f/#=0.95) was chosen as the objective camera lens to ensure the appropriate magnification. Overall, the imaging system provided a picture of the cell with the scale of 42.8 $\mu$m/pixel.

All the components are fastened to an optical bench plate of $900 \times 600\,mm^2$, and the entire interferometer is enclosed in a box made of insulating material 3 cm thick. An air-to-air heating/cooling assembly of Laird (part no. AA-040-
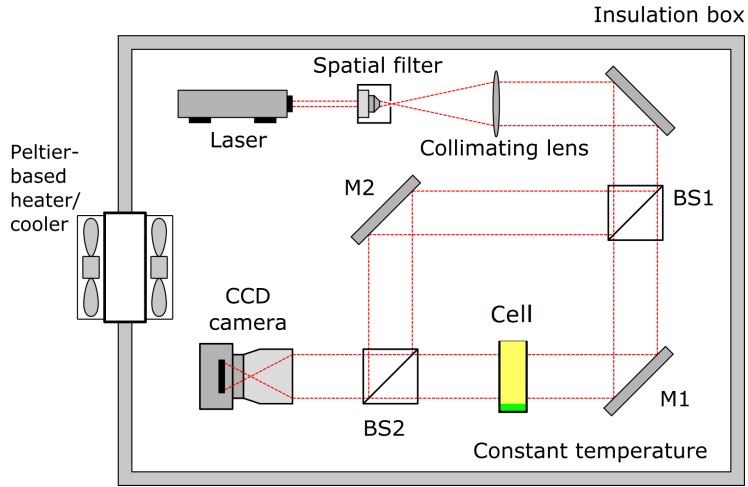
Figure 1: Schematic of the Mach-Zehnder interferometer used to measure the vapor concentration.

12-22-00-00) has been incorporated into one of the box walls. The assembly was driven by dedicated PID controller of Laird (part no. PR-59). The temperature feedback to the controller was implemented by a calibrated precision NTC thermistor, which has been in permanent contact with a metallic holder of the test cell.

Such an arrangement has solved three problems at once. First, it provides a constant and monitored temperature of the ambient gas around the cell with ability to regulate this temperature in a certain range. Second, it maintains the interferometer at constant temperature throughout the experiment, thereby eliminating its possible temperature drift. Third, the fan of the inner heat-sink of the heating/cooling assembly ensures an airflow around the cell, fast enough for removing the vapor reaching the open top of the cell. This airflow can cause a slight jitter of the fringe contrast. However, after the numerical reconstruction of the interferograms, we did not observe any notable rise in the optical phase noise.

The Hellma cells, being specially designed for optical measurements, features high-quality glass walls with very well characterized dimensions. The commer-

cially available standard absorption cell of Hellma, QS 100-10-40, fits well to
the size of all our optical elements. Characteristic sizes of the cell, critical for
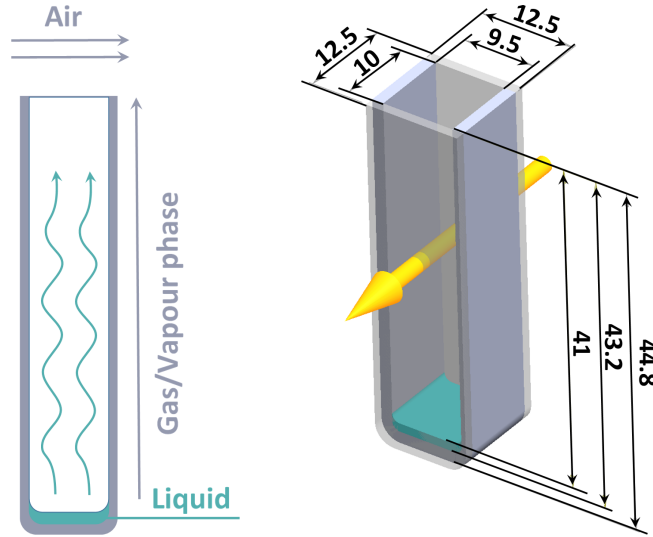the study, are indicated in Fig. 2.



Figure 2: Schematic of the experimental cell and its 3D drawing with indication of all critical
sizes. The arrow indicates the direction of the laser beam.

2.3. Experimental procedure

A typical approach, widely used in previous works [27, 32] is to monitor the
descending level of the interface during evaporation, from which the evaporation
rate and vapor diffusion coefficient are derived. To ensure accurate measure-
ments, it is necessary to fill the diffusion tube with a significant amount of
liquid. A moving interface makes the process unsteady and requires appropri-
ate adaptation of the analytical solution describing the problem. In our case
with a relatively short diffusion tube, the procedure was modified to keep the
diffusion path as long as possible.

To do so, a small amount of liquid is injected so that the initial height of
the liquid layer is much smaller than the total cell height. Liquid is carefully
injected by a Hamilton syringe, Gastight® #1725 LT (volume $250\,\mu$l, scale

division 5 $\mu$l), that allows an accurate control of the liquid sample volume. The volume was always constant and equal to $0.20 \pm 0.002$ ml. The resulting height of the liquid in the cuvette varied slightly depending on the temperature of the experiment and was $\approx 2.2$ mm. The meniscus was formed after the filling process at the contact line between the liquid-gas interface and the cell walls and made a small part of the gas phase adjacent to the interface invisible to optics, which, however, did not disrupt data processing. Although the presence of a meniscus could potentially affect the outcome, we did not expect a noticeable impact, so, we neglected it. Since the vapor flux was measured by estimating the total time of the complete sample evaporation, this approach requires a tiny amount of liquid for measurement. The efficiency of the chosen approach was well confirmed in the very first tests (see the beginning of Sect. 3 for details).

The smallness of the sample is especially important as the liquid evaporates into a closed box. The volume of the box is rather large comparing with the cell's volume (80 l vs. 4 ml), which makes it possible to neglect the residual vapor concentration in the surrounding air. Nevertheless, after the end of each experimental run, the box was carefully vented with the conditioned air of laboratory to eliminate the vapor leftover from a previous experiment.

### 2.4. Optical phase extraction

We are interested in the variation of the refractive index caused by evaporation. In optical interferometry, an interferogram with useful optical information is always processed relative to a reference one taken before the refractive index changes. This reference image is afterwards subtracted from each of the subsequent images to identify the characteristics of interest. The reference image is the first recorded interferogram when the liquid is not injected yet. In this case, the beam passes only through air and walls of the cell. The reference image includes three contributions in a phase shift: optical elements along the beam path, non-uniform air temperature and the temperature distribution in glass walls (if any). The following images are acquired after liquid injection (Fig. 3(a)). Its evaporation leads to a change in the refractive index over the

experimental cell. These images contain two more important contributions: the temperature and the concentration distributions in the gas phase. When all interferograms are recorded, the image processing starts. We follow the previously developed procedure of image processing [35, 36]. Each grey-scale image is read by a Python script as a 2D array of pixels of different intensity, from 0 to 255 (a value of 0 represents black and a value of 255 represents white). Fringes in the images are well distinguished; a magnified fringe pattern is shown in Fig. 3(b). Fringe spacing is about 4-5 pixels. An example of the initial intensity distribution is shown in Fig. 3(c) over the horizontal line.

2D Fourier transform is applied to all the images to get an optical phase at each pixel. This procedure is equally applied for the reference and objective images. A typical intensity distribution in Fourier space is shown in Fig. 3(d) on which one can distinguish bright spots. Spots represent the first-order intensity peaks while zero-order one is placed in the corners of the images. To proceed, the position of the peaks in the Fourier space should be changed. The 2D Fourier transform output is rearranged by moving the spectrum on $f_{x0}$ toward the origin of Fourier domain (Fig. 3(e)). The zeroth-order peak $I(f_x, f_z)$ gives the amplitude information, which is not of interest to us, while the first-order peaks $C(f_x - f_{x0}, f_z)$ and $C^*(f_x + f_{x0}, f_x)$ carry equal information about the phase shift - see Fig. 3(e). The zeroth-order peak is right in the center and the first-order peaks are located on the sides (Fig. 3(f)). In the ideal case, each peak would be represented by one point. But because of inaccuracies in the interferometer, such as tension in optical elements and non-ideally adjusted tilting angle, peaks are broadened in some area. To discard the zeroth-order peak, a dedicated filter was made for this region using an inverse Gaussian. After application of the filter to the original image, the zeroth-order peak disappears. Then, any peak of the first order can be used for further processing, and the second one should be deleted. The remaining first-order peak should be placed in the center of the image before proceeding. For this, a new filter is created and applied to all the images, and only one peak remains in them, as shown in Fig. 3(g).
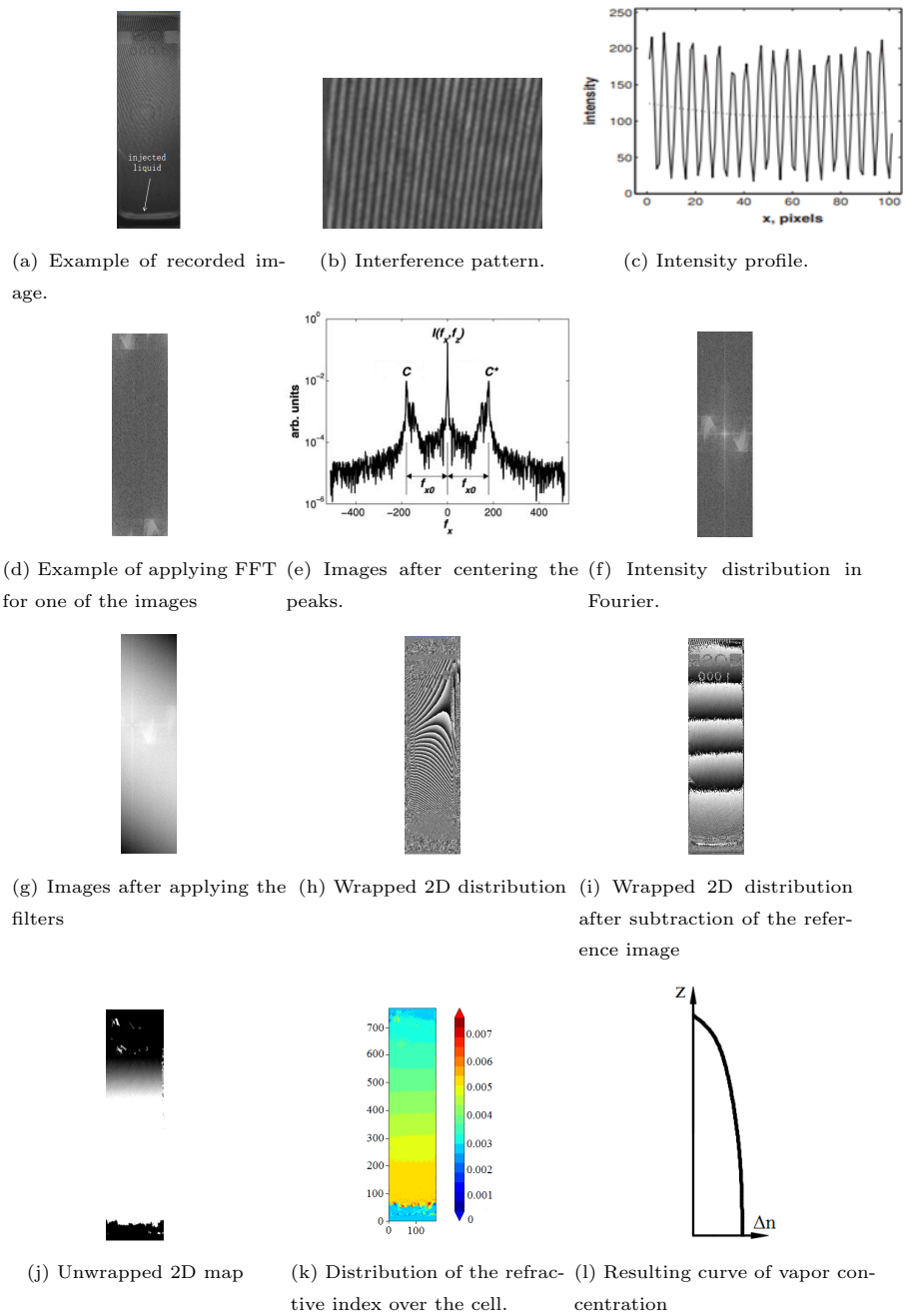
(a) Example of recorded image.



(b) Interference pattern.



(c) Intensity profile.



(d) Example of applying FFT for one of the images



(e) Images after centering the peaks.



(f) Intensity distribution in Fourier.



(g) Images after applying the filters



(h) Wrapped 2D distribution



(i) Wrapped 2D distribution after subtraction of the reference image



(j) Unwrapped 2D map



(k) Distribution of the refractive index over the cell.



(l) Resulting curve of vapor concentration

Figure 3: Steps of the optical phase extraction.

In the next step, an inverse FFT is applied to the pre-processed reference and objective images. Then the reference image is subtracted from all the objective images to get rid of non-informative contributions. After this step, it is even possible to recognize by eyes the optical phase change due to the concentration and temperature variations as seen in Fig. 3(i). But the phase is wrapped, which means that it belongs to the range $(-\pi; \pi)$ after inverse FFT. The following step is the application of the phase unwrapping algorithm. The algorithm searches and eliminates the discontinuities which are represented by $2\pi$ phase jumps between two nearby pixels. The unwrapped phase map is shown in Fig. 3(j).

The obtained optical phase variation $\Delta\varphi$ is recalculated into the refractive index as

$$\Delta n = \Delta\varphi \frac{\lambda}{2\pi L_{opt}} \tag{1}$$

where $\lambda$ is the wavelength of the probing laser beam, and $L_{opt} = 10.0\,\text{mm}$ is the path-length of the light beam inside the Stefan cell.

The final step in the optical information analysis is the elimination of the absolute value ambiguity, as the phase and refractive index maps obtained by the above way are always relative. This is done presuming that at the open end of the tube the vapor concentration is always zero, and temperature disturbances are absent there. Then, all vertical profiles are normalized in a way to anchor the value at the very top pixel to zero.

## 3. Results and discussion

### 3.1. Diffusive regimes observed during the course of experiment

Using interferometric measurements, we have identified three temporal regimes of vapor diffusion, occurring at different times of the experiment and with different duration. These regimes are clearly distinguished on the plot of the temporal evolution of the full refractive index difference $\Delta n$, shown in Fig. 4 and detailed in Fig. 5. Figure 5 presents the distribution of the refractive index with the cell height. Since the obtained two-dimensional refractive index maps change mainly in the vertical direction, we select for further analysis one representative

profile in the vertical direction, which is obtained by averaging over a strip of
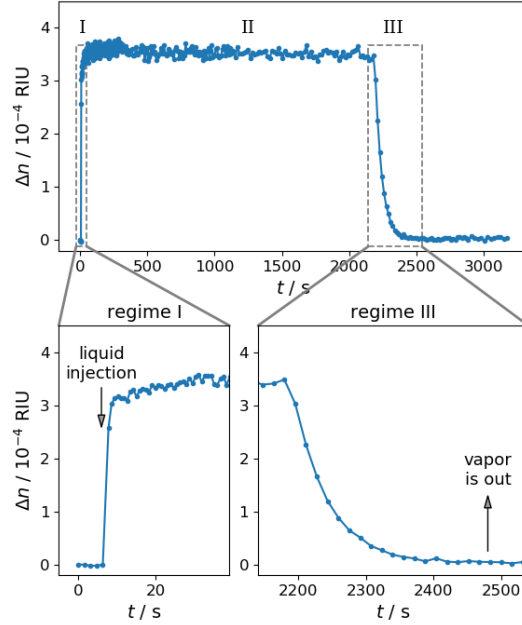10 pixels wide along the central axis.



Figure 4: Distinct regimes appearing in the course of a typical experiment. Two callouts show the regimes I and III with different time scales. The plotted case corresponds to evaporation of acetone at the ambient temperature of $T = 313.15\,\text{K}$.

Regime I corresponds to the time interval between the start of the liquid injection into the cell and establishing of a steady vapor concentration profile. As may be seen in the callout to Fig. 4 corresponding to regime I, it lasts a very short time, i.e. a few seconds. During this regime the vapor concentration (corresponding to the refractive index shown) almost immediately reaches the saturation level at the interface, and then the vapor travels to the open end of the cell until a steady profile is established. The distribution of the refractive index profiles $n(z)$ over the cell height at different times is shown in Fig. 5. In

13

<sub>267</sub> total, the establishment of a steady profile takes less than 20 s.
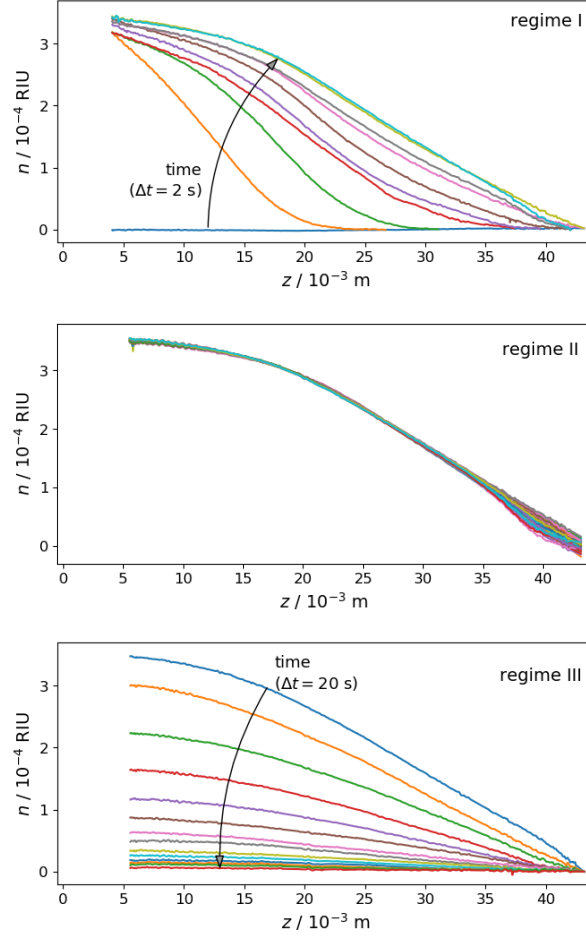


Figure 5: Time evolution of the refractive index profiles for three regimes distinguished in Fig. 4 in experiments with acetone at $T$=313.1 K. For each point in time, one representative profile in the vertical direction is displayed, which is obtained by averaging over a strip of 10 pixels wide along the central axis. Note that variations in the refractive index directly correspond to the behavior of the vapor concentration.

<sub>268</sub>    Regime II starts when both the total refractive index difference $\Delta n$ and the
<sub>269</sub> refractive index profiles $n(z)$ are practically frozen. Figure 5b shows that all
<sub>270</sub> the $n(z)$ profiles obtained at different times merge into one curve, except for the

14

region near the top of the cell. This regime, characterized by an almost perfect steady state, ends up with an abrupt drop of $\Delta n$, which logically corresponds to the complete evaporation of the liquid. A noticeable presence of $\Delta n$ oscillations during this regime can be seen in Fig. 4. However, Fig. 5 demonstrates that the region in which these fluctuations occur is limited, and located at the very top of the cell. The reason for the existence of such localized fluctuations is discussed in detail in section 3.4.2.

Regime III begins at the moment when there is no more liquid to feed a steady vapor distribution inside the cell, and it ends when the vapor completely leaves the cell and the refractive index distribution thus returns to its original state. The slow decrease in the level of the refractive index profiles with time (vapor concentration) in this regime can be traced in Fig. 5c.

While it is possible to use each of these regimes for the extraction of the diffusion coefficient, we chose the regime II for at least two reasons. The steady profiles allow not only fitting them to an existing analytic solution to determine the vapor diffusion coefficient, but also to evaluate the optical properties of the vapor-air mixture, provided that the saturation vapor pressure is known.

*3.2. Evaluation of evaporation rate and interfacial temperature*

*3.2.1. Evaporation rate*

A typical approach to measuring the evaporation rate in the configuration of the Stefan tube is to monitor the lowering rate of the liquid-vapor interface. Here, we use a different way to measure the evaporation rate, namely, by estimating the time required for the complete evaporation of the injected liquid. This time interval corresponds to the duration of the regime II, and can be accurately extracted from the experimental record, e.g., see Fig. 4.

The measured evaporation time $t$ allows the calculation of the evaporation rate

$$N_v = \frac{\tilde{n}}{t \cdot S} \tag{2}$$

where $\tilde{n} = \rho V / M_v$ is the number of moles of the evaporating liquid, $\rho$ is its density, $M_v$ its molar mass, $V = 0.20\,\mathrm{ml}$ is the volume of injected liquid sample.

15

The evaporating surface is assumed to be plain, without menisci, and measures $S = 9.25 \times 10.0\,\mathrm{mm}^2$.

Measurements were carried out with two liquids in the temperature range from 283.13 to 313.15 K and the results are summarized in Table 2. The same values of evaporation rate, but expressed in mass units instead of moles, are given in Table S2 in Supplementary Material.

Table 2: Temperature $T/\mathrm{K}$; number of moles of the evaporated liquid $\tilde{n}/10^{-3}\,\mathrm{mol}$; optically-measured total time of evaporation $t/\mathrm{s}$; and evaporation rate $N_v/10^{-3}\,\mathrm{mol\,s^{-1}\,m^{-2}}$ for acetone and HFE-7100.

| $T$ | $\tilde{n}$ | $t$ | $N_v$ |
|---|---|---|---|
| *Acetone* | | | |
| 283.15 | 2.76 | 8400 | 3.55 |
| 288.15 | 2.74 | 6500 | 4.56 |
| 293.15 | 2.72 | 4800 | 6.13 |
| 298.15 | 2.70 | 3900 | 7.48 |
| 303.15 | 2.68 | 3000 | 9.66 |
| 308.15 | 2.66 | 2600 | 11.1 |
| 313.15 | 2.64 | 2150 | 13.3 |
| *HFE-7100* | | | |
| 283.15 | 1.21 | 12500 | 1.05 |
| 288.15 | 1.20 | 9900 | 1.31 |
| 293.15 | 1.19 | 7700 | 1.67 |
| 298.15 | 1.19 | 6300 | 2.04 |
| 303.15 | 1.18 | 5050 | 2.53 |
| 308.15 | 1.17 | 4000 | 3.16 |
| 313.15 | 1.16 | 3050 | 4.11 |

For both liquids, the temperature dependence of the evaporation rate is well

16

described by second-order polynomials

$$N_v(\text{Ace}) = 7.64 \cdot 10^{-3} + 3.28 \cdot 10^{-4}(T - T_0) + 3.31 \cdot 10^{-6}(T - T_0)^2$$

$$N_v(\text{HFE}) = 2.03 \cdot 10^{-3} + 9.81 \cdot 10^{-5}(T - T_0) + 2.40 \cdot 10^{-6}(T - T_0)^2 \qquad (3)$$

with the reference temperature $T_0 = 298.15\,\text{K}$. The region of validity of the given correlations is $\pm 15\,\text{K}$ around the reference point. The convenience of this form of polynomial representation is that the free term gives directly the evaporation rate at the reference temperature.

The experimental data points and correlations are presented in Fig. 6.
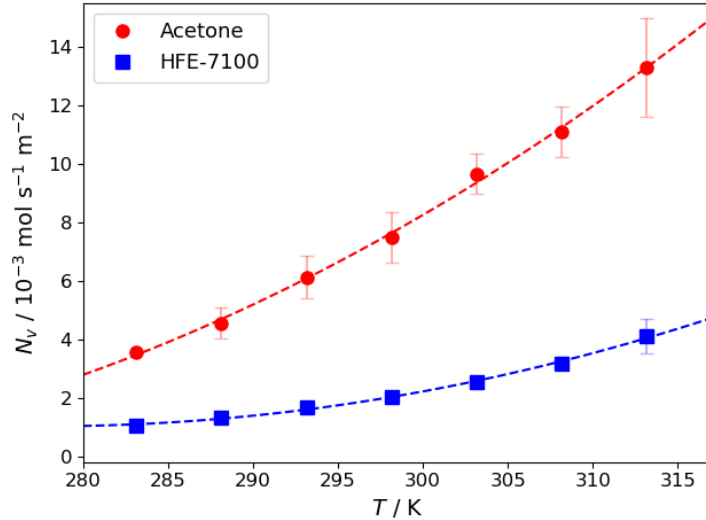


Figure 6: Dependence of the experimental evaporation rate on temperature for acetone and HFE-7100. The error bars are standard deviations.

The evaporation rate in both liquids increases by about four times with an increase in temperature by $\Delta T = 30\,\text{K}$. In addition, Fig. 6 indicates that acetone has a larger rate of the increase with temperature compared to HFE-7100. Each presented data point is obtained by averaging over two to four tests and the error bars are also shown in Fig. 6. Among the three parameters in Eq. (2), the evaporation time $t$ exhibits the largest scattering, reaching upper

17

limit 7% for HFE-7100 and of 12% for acetone. Since the errors in defining $\tilde{n}$ and $S$ are much less, the error specific to $t$, is transmitted to the error of $N_v$.

### 3.2.2. Temperature drop on the gas-liquid interface

Evaporation induces a cooling of the liquid–gas interface. In order to calculate the temperature drop at the interface caused by evaporation, we consider the problem of stationary conductive heat transfer along the cell. Assuming adiabatic sidewalls, heat propagates in a one-dimensional manner from the bottom and top of the cell (both are at the ambient temperature) towards the interface, which acts as a heat sink due to evaporation. Our experimental approach allows to precisely calculate the heat absorbed by the evaporating interface. The evaporation rate was characterized in the previous section (see 3.2.1), but for the thermal properties the mass units are used, i.e., $N_v = m/t \cdot S$. Here $m$ is the mass of the evaporated substance which is known, since its volume is precisely dosed. With the data on latent heat of vaporization available in the literature [37, 38], the evaporative heat flux can be estimated as $Q = \Delta_v H \cdot N_v$. After determining the evaporative heat loss, the problem can be solved analytically with respect to the interface temperature (see details in the Supplementary Material).

All the results related to the temperature drop for the experiments performed are summarized in Table S2 of the supplement, and here we suggest some conclusions. First, the effect is not large; in all the cases the temperature drop is limited to the range $0.9 < |\Delta T_{calc}| < 5.9\,\mathrm{K}$, and, as expected, it is more pronounced at higher temperatures. Second, the thermal effect of acetone is noticeably higher than that of HFE-7100. Thus, in experiments with acetone, one can expect large disturbances of a thermal nature.

### 3.3. Optical properties of vapor–air mixtures

The interferometry measures the combined effect of concentration and temperature. For the given wavelength, the variation of the refractive index $\Delta n$ is

caused by the variations of the vapor concentration $\Delta x_v$, and the vapor temperature $\Delta T$

$$\Delta n = \left(\frac{\partial n}{\partial x}\right)_{p,T} \Delta x_v + \left(\frac{\partial n}{\partial T}\right)_{p,x} \Delta T \qquad (4)$$

The relation includes the so-called *optical contrast factors*, $\left(\frac{\partial n}{\partial x}\right)_{p,T}$ and $\left(\frac{\partial n}{\partial T}\right)_{p,x}$, which are the concentration- and temperature-related factors, respectively. These contrast factors are the characteristics of the medium, and can be independently measured or calculated. In what follows, for ease of notations, we omit the subscripts indicating the conditions at which the contrast factors are obtained.

The applied approach is aimed not only at obtaining the vapor concentration, but also at comparing the measured $\Delta n_{exp}$ with its analogue $\Delta n_{calc}$, calculated mostly on the basis of external information. This allows to estimate the accuracy of theoretical predictions of the optical properties of the vapor-air mixtures as well as consistency of the experimental measurements.

We begin with an example of evaluation of the experimental and of calculated optical properties of vapor-air mixtures such as $\Delta n$ used in this work. Figures 4 and 5 show that for acetone at $T = 313.15\,\text{K}$ the total refractive index difference between the liquid interface and the open top is roughly $\Delta n_{exp} = n_{z=b} - n_{z=H} \approx 3.5 \cdot 10^{-4}$ at the steady state. To calculate $\Delta n_{calc}$ using Eq. (4), one needs to evaluate four quantities in total: two optical contrast factors, concentration and temperature differences along the cell's height. The concentration difference is estimated directly, because the concentration at the interface is determined by the saturated vapor pressure, while it is zero at the top of the air-purged cell, $\Delta x_v = x_v^\circ - 0 = p_s/p$. Here $p_s$ is the saturation vapor pressure, with its temperature dependence available in literature for both liquids [39, 38], and $p = 101\,325\,\text{Pa}$ is the ambient pressure. Both the saturation vapor pressure $p_s$ and corresponding vapor concentration $x_v^\circ$ are tabulated for all the tested temperatures in the Supplementary Material. The temperature drop was investigated in the section above, and the only remaining unknowns in Eq. (4) are the contrast factors.

19

*3.3.1. Refractive index*

The Lorentz–Lorenz equation is widely used for the description of a refractive index $n$ of pure transparent substances through their effective molecular polarizability $\alpha$:

$$\frac{n^2-1}{n^2+2} = \frac{4\pi}{3}N\alpha, \quad \text{or,} \quad \frac{n^2-1}{n^2+2} = \frac{4\pi}{3}\frac{\rho N_A}{M}\alpha, \tag{5}$$

where $N$ is the number of molecules of the substance per unit volume, $N_A = 6.022 \times 10^{23}\,\text{mol}^{-1}$ is the Avogadro constant, $\rho$ is the density (mass per unit volume), and $M$ is the molar mass. When the polarisability is small and the square of the refractive index is $n^2 \approx 1$, which holds for many gases, Eq. (5) reduces to:

$$n^2 - 1 \approx 4\pi N\alpha$$

or, under condition of $n + 1 \approx 2$, it turns into the Gladstone–Dale expression:

$$n - 1 \approx 2\pi N\alpha = 2\pi\frac{\rho N_A}{M}\alpha. \tag{6}$$

To obtain the concentration dependence of the refractive index, Eqs. (5) and (6) can be extended for mixtures by assuming a linear additive rule for the polarizability [40, 41]

$$n - 1 = 2\pi N_A \rho_t \sum_{i=1}^{n} \frac{w_i \alpha_i}{M_i}, \tag{7}$$

where $w_i$, $M_i$, and $\alpha_i$ are the mass fraction, the molar mass, and the molecular polarizability of component $i$, respectively, and $\rho_t$ is the mass density of the mixture. Converting the concentration into mole fractions $x_i$, the expression now takes the following form:

$$n - 1 = 2\pi N_A c_t \sum_{i=1}^{n} x_i \alpha_i, \tag{8}$$

where $c_t$ is the molar density of the mixture $(\text{mol/m}^3)$ defined as

$$c_t = \frac{p}{RT} \tag{9}$$

where $p$ is the total (here atmospheric) pressure (Pa), $T$ is the absolute temperature (K), and $R = 8.314463 \, \mathrm{m^3 \, Pa \, K^{-1} \, mol^{-1}}$ is the gas constant. Finally, the formula for the refractive index of the vapour-air mixture is

$$n = 1 + 2\pi N_A \frac{p}{RT} \left[ \alpha_a + x_v(\alpha_v - \alpha_a) \right] , \tag{10}$$

where the subscript 'a' corresponds to air and the subscript 'v' to vapour.

### 3.3.2. Optical contrast factors

The optical contrast factors are calculated taking the derivatives of Eq. (10), as shown in the Supplementary Material. We found that the thermal contribution into the entire $\Delta n_{calc}$, the second term in Eq. (4), is small and varies in the range from 1.1 to 3.5 % of the concentration part. This finding allows us to safely neglect the temperature input into the refractive index (second term in RHS of Eq. (4), and to estimate of the concentration contrast factor directly from the experiment, as

$$\left( \frac{\partial n}{\partial x} \right)_{exp} = \frac{\Delta n_{exp}}{x_v^\circ} \tag{11}$$

Both, calculated $\Delta n_{calc}$ and experimental $\Delta n_{exp}$ are presented in Fig. 7 and their values are given in Table S3 of Supplementary Material.

Figure 7 shows that a theoretical approach to evaluate the contrast factors of vapor-air mixtures works very well at room temperature and above, while at lower temperatures, the agreement with experiment is less good. The difference between the theoretical and experimental values is temperature-dependent and varies between 0 to 20 % approximately. For all the temperatures, the ratio of the experimental and calculated values is of the same order for both liquids.

Another important result is the demonstrated consistency of our measurements with the available literature data on the molecular polarizability of pure substances, their saturation vapor pressure, and other thermophysical properties. This consistency justifies using of the experimentally determined concentration contrast factors in the next part of the paper, when needed.
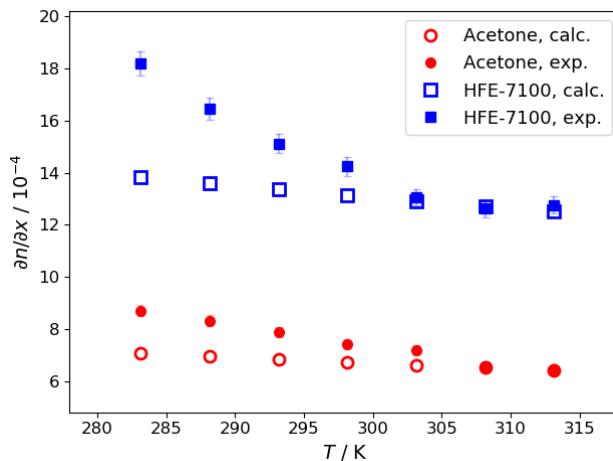
Figure 7: Calculated and measured optical concentration-related contrast factor ($\partial n/\partial x$) for the vapor-air mixture of acetone and HFE-7100 over examined temperature range.

### 3.4. Diffusion coefficients of vapors in air

#### 3.4.1. Governing equations

The diffusion problem is treated using the so-called "diffusion through a stagnant gas film" model which is a well described in [42]. In the frame of this model, the evaporating substance is moving up (diffusing) through a gas "film" (i.e., a gas layer) which is stagnant (not moving). At steady state, the air flux in the diffusion tube is absent (provided that the solubility of air in the liquid is negligible). We consider this assumption perfectly valid in our case, as we always used non-degassed liquid in experiments, and the tiny amount of the liquid sample does additionally guarantee an absence of any measurable air dissolution in the liquid.

The total flux of diffusing vapor, $N_v$, consists of convective and diffusive parts, as

$$N_v = x_v \left( N_v + N_a \right) - cD \frac{\partial x_v}{\partial z} \tag{12}$$

where $x_v$ is the vapor concentration in mole fractions; $N_v$ and $N_a$ are the vapor and air fluxes, respectively, $(\mathrm{mol\,s^{-1}\,m^{-2}})$; $c$ is the total molar concentration of the gas, $(\mathrm{mol\,m^{-3}})$ and $D$ is the vapor diffusion coefficient $(\mathrm{m^2\,s^{-1}})$. In the

22

ideal gas approximation, the total concentration $c$ is given by Eq. (9). Since the air is stagnant (i.e., $N_a = 0$), Eq. (12) turns into

$$N_v(z) = -\frac{cD}{1 - x_v}\frac{\partial x_v}{\partial z} \tag{13}$$

When the system reaches a steady state, with no concentration change in time, the spatially-invariant vapor flux can be written as

$$-\frac{dN_v(z)}{dz} = 0 \quad \rightarrow \quad \frac{d}{dz}\left(\frac{cD}{1 - x_v}\frac{dx_v}{dz}\right) = 0 \tag{14}$$

With general boundary conditions, $x_{v1} = x_v(z_1)$ and $x_{v2} = x_v(z_2)$, the solution of Eq. (14) takes form (for details see in [42]):

$$\left(\frac{1 - x_v(z)}{1 - x_{v1}}\right) = \left(\frac{1 - x_{v2}}{1 - x_{v1}}\right)^{\frac{z - z_1}{z_2 - z_1}} \tag{15}$$

In our case, with zero vapor concentration at the top of the cell, $x_{v2} = 0$ at $z_2 = H$, and the saturation concentration at the interface, $x_{v1} = x_v^\circ$ at $z_1 = b$, the solution is reduced to

$$x_v(z) = 1 - (1 - x_v^\circ)^{\frac{H - z}{H - b}} \tag{16}$$

Using Eq. (16) one can find an explicit expression for the derivative $\frac{\partial x_v}{\partial z}\big|_{z=b}$, to substitute in Eq. (13). This leads to an expression bounding the diffusion coefficient with the evaporation rate $N_v^\circ$ and the thickness of the stagnant gas layer $(H - b)$ as

$$N_v^\circ = \frac{cD}{H - b}\ln\left(\frac{1}{1 - x_v^\circ}\right) \tag{17}$$

The vapor concentration at the interface, $x_v^\circ$, can be derived from the saturation vapor pressure $p_s$ at a given temperature as $x_v^\circ = p_s/p$. The working equations for $p_s$ are available in the literature for a wide range of liquids, and for acetone it is given by the Antoine equation [39]

$$\log_{10}(p_s[\text{bar}]) = 4.4245 - \left(\frac{1312.25}{T[\text{K}] - 32.45}\right) \tag{18}$$

and for HFE-7100 by equation [38] :

$$\ln(p_s[\text{Pa}]) = 22.415 - \left(\frac{3641.9}{T[\text{K}]}\right) \tag{19}$$

The saturation vapor pressure for acetone and HFE-7100 is tabulated in Table S3 of Supplementary Material, and the corresponding vapor concentration (in molar fractions) is given in section 3.4.3, see Table 3.

It is worth mentioning also that the interfacial evaporation rate $N_v^\circ$ is equivalent to the time-averaged evaporation rate $N_v$, see Eq. (3) in section 3.2.1. The latter one was measured as a global rate in a steady state, but due to 1D character of the problem and the invariance of the vapor flux along $z$-axis (cf. Eq. (14)), it is equivalent to the former.

Recall that Eq. (17) is obtained under condition of the motionless interface. An alternative expression that considers the movement of the interface due to evaporation does exist as well [42], and it requires monitoring of the interface position with time [27]. In our experiments, the liquid layer was intentionally chosen to be small compared to the total cell height, $b \ll H$, so that the interface motion can be neglected.

In total, four quantities are needed to calculate the diffusion coefficient out of Eq. (17). Among them three quantities were determined above: the gas concentration $c$, the saturation vapor concentration $x_v^\circ$, the evaporation rate $N_v^\circ$. The remaining quantity is the diffusion path length. One may assume that the vapor diffusion path is fixed by the cell geometry and is equal to $H - b$. However, this approach may lead to an essential error in the diffusion coefficient which is discussed in the next section.

### 3.4.2. Experimental concentration profiles and diffusion path length

The observed profiles of the vapor concentration inside the diffusion tube are expected to closely follow their theoretical shape, outlined by Eq. (16). We have found, however, that in all conducted experiments it was never the case.

One of the typical situations is illustrated in Fig. 8. The solid curve presents the experimental results obtained in regime II, when the refractive index is converted to concentration. Accordingly, the shape of the curve is similar to that one in Fig. 5, but taken for another temperature. The dash-dotted curve is the theoretical curve according to Eq. (16) where $x_v^\circ$ is the saturation va-
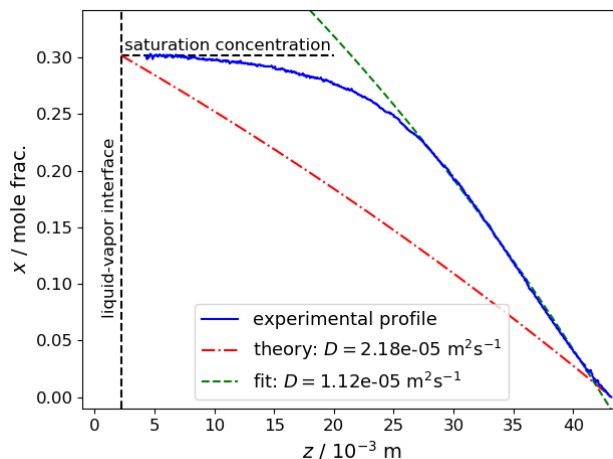
Figure 8: The distribution of vapor concentration along the cell obtained with different raw approaches: the experimental curve (solid), the theoretical curve according to Eq. (16) (dash-dotted) and the curve obtained by fitting (dashed).

por pressure, and $H$ and $b$ are taken from the experiment after filling the cell. This theoretical curve connects the two pivot points of the system: the saturated vapor concentration at the liquid-vapor interface and the vanishing vapor concentration at the top of the cell. Obviously, apart from these two points, this curve has nothing more in common with the actual vapor concentration in the tube. Furthermore, the diffusion coefficient obtained from this curve (and shown in the legend) is twice that of the literature data. At the same time, we have noticed that there exists an extended region with the constant slope on the experimental profile. Targeting only this part of the experimental profile, we limited the region $z_1 < z < z_2$ (e.g., $z_1$=25 mm and $z_2$=41 mm) and fitted Eq. (15) to the experimental data using $x_v^\circ$ as the fit parameter. The results of this fit (shown by the dashed curve) are in line with the experiment and provide a reasonable value for the diffusion coefficient.

Figure 8 evidences that the experimental curve may be divided into regions, where it either coincides with the analytical solution or deviates from it. Thus, the next task is to identify perturbed regions and determine the cause of their

25

occurrence. Comparison of the experimental and fitting curves shows visible deviations at two extremes. A tiny divergence occurs at the very top of the cell, $41 < z < 43\,\mathrm{mm}$, and a noticeable deviation occurs in the lower part of the cell, $z < 25\,\mathrm{mm}$.

The reason for the disturbance at the top of the diffusion cell is fairly easy to identify, it is caused by the air flow around the cell, as discussed in Sec. 2. The air flow may partly propagate into the cell volume causing deformation of the concentration profile at the very top. The deviation near the bottom is much stronger and the reason is not so obvious.

Upon closer examination of Fig. 8 it can be seen that the vapor concentration changes only slightly within the lower third of the cell height. This observation contradicts the assumed diffusive transport in the region, and can be explained by mixing due to convection in the gas, even if rather slow. Identifying a possible source of convection in the gas does not pose a problem, since it can be triggered by Marangoni convection at the liquid interface. As demonstrated in section 3.2.2 and in Supplementary Material, evaporation causes a small, but not negligible drop in temperature at the interface. Due to imperfect boundary conditions at the lateral walls, this thermal effect can be non-uniform along the interface, resulting in Marangoni flows strong enough to drive the gas motion.

The used digital interferometry enables the tracing the evolution of the concentration field in time in the entire 2D region. Figure 9a shows distribution of the wrapped phase in a typical image. It is clearly seen that in the upper half of the cell, the isolines of the wrapped phase are horizontal, which evidences 1D mass transfer in the region. In contrast, the isolines in the lower part are concave towards the interface, which confirms the hypothesis of the presence of convection in the region. It is worth noting that such phase maps were rather common in experiments, especially in the case of acetone.

Summing up the above considerations, along the experimental cell, we have identified three regions with different transport mechanisms which are depicted in Fig. 9b. The self-explanatory sketch demonstrates that the pure diffusive mechanism takes place only in the limited part of the cell, which is completely

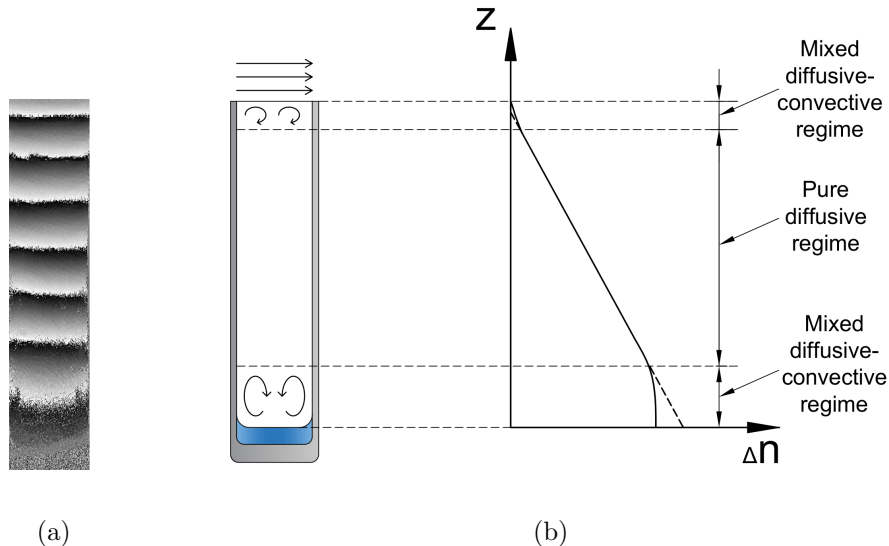Figure 9: (a) Wrapped optical phase map corresponding to evaporation of acetone at $T = 308.15\,\mathrm{K}$. (b) Revealed mechanisms of vapor transfer through the cell.

free of convective disturbances of various origins. This calls for a specific adaptation of the data extraction procedure.

Two ways can be suggested to overcome this problem. The first one, already implemented for the dashed curve in Fig. 8, uses the limiting concentrations $x_v^\circ$ as free fit parameter. This approach is somewhat artificial, and results in arbitrary values of the limiting vapor concentrations at the interface and the cell's top. In what follows, we omit this approach.

The second option retains the correct limiting concentrations, but requires an estimate of the "true" (or effective) diffusion path in the system as illustrated in Fig. 10. Regions prone to convection are cropped out and the stagnant gas layer is considered true over distance $L_{\mathrm{eff}}$. Then the experimental data are fitted to the analytical solution only in this layer. For this, the initial thickness of the gas layer $(H - b)$ should be replaced by its effective analogue $L_{\mathrm{eff}}$ in Eq. (17).

Next, we determined the effective diffusion path in all the conducted experiments, and these data are presented by symbols in Fig. 11. Interestingly,

27

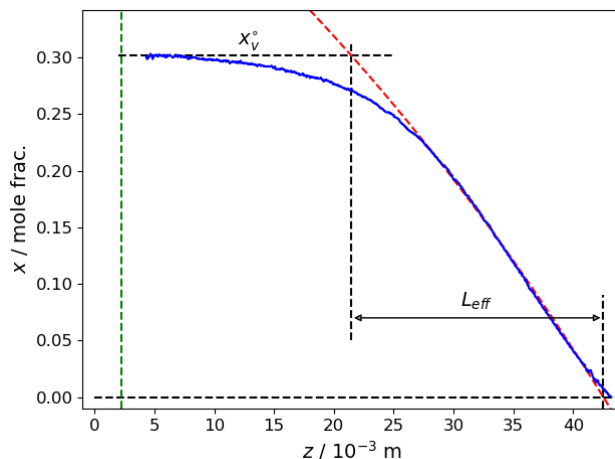Figure 10: Determination of the cell length ($L_{\text{eff}}$) where the diffusive transport mechanism occurs. The large region in the lower part is presumably affected by Marangoni convection. The tiny region at the top is perturbed by the ambient air flow.

the effective diffusion path increases with temperature, which means that the region adjacent to the interface and disturbed by convection does contract with increasing temperature. This contraction is especially noticeable in the case of acetone.

The data of the effective diffusion path is used to determine the diffusion coefficient and, looking at the possible trend curves in Fig. 11, we see that they are slightly scattered. So, we search a polynomial interpolation of the obtained $L_{\text{eff}}$ and further use the $L_{\text{eff}}$ value from this polynomial, rather than the one directly obtained from the experiment.

We have interpolated the data on $L_{\text{eff}}$ by power series polynomials of the lowest possible order so that the interpolation curve remains within the measurement error. A careful estimate of the corresponding error-bars for acetone is 10%, which limits the polynomial power to quadratic. In the case of HFE-7100 the error-bar is much smaller, 1.8% only, which requires the polynomial of third order to fit. We do not provide these polynomials explicitly as they do not have a special value, but the values of interpolated $L_{\text{eff}}$, used for calculation of the
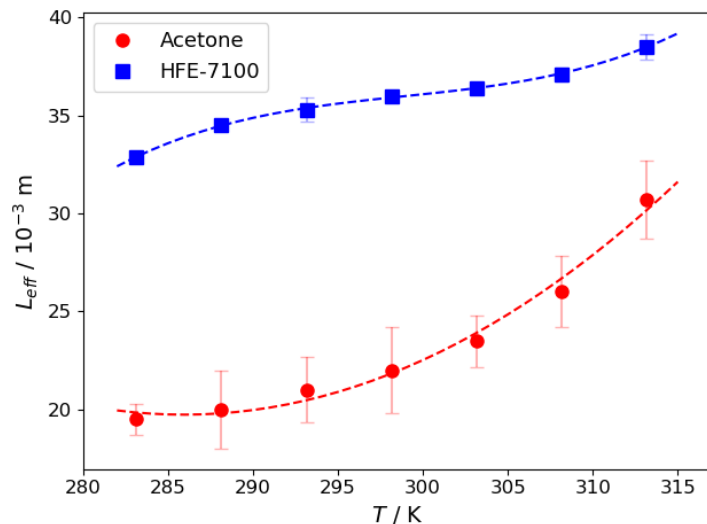
28

Figure 11: Temperature dependence of the effective diffusion length $L_{\mathrm{eff}}$. The symbols indicate points obtained from fitting of experimental results, and the dashed curves represent the polynomial interpolation: the second order for acetone and the third order for HFE-7100. The interpolated values will be used to determine the vapor diffusion coefficients of acetone and HFE-7100 in air. The error bars are standard deviations.

diffusion coefficients, are given in Table 3.

### 3.4.3. Diffusion coefficients

At this point, all the quantities required to calculate the diffusion coefficient using Eq. (17) have been determined, they are $x_v^\circ$, $N_v^\circ$, $L_{\mathrm{eff}}$. Before placing them in the final table, they were approximated by power polynomials in order to reduce the possible scattering of the resulting diffusion coefficients. For example, the evaporation rate $N_v^\circ$ was not taken from Table 2, instead, it was calculated by interpolation polynomials Eq. (3). Similarly, the effective diffusion length was not taken from experimental points in Fig. 11, but from the interpolation curves shown there. All these improved data are summarised in Table 3.

Since we care about the quality of the initial data, the correct estimation of the net error of the diffusion coefficient is important. Among the three param-

29

Table 3: Saturation vapor concentration $x_v^\circ / \mathrm{mol\,mol^{-1}}$, evaporation rate $N_v^\circ / 10^{-3}\,\mathrm{mol\ s^{-1}\,m^{-2}}$, effective diffusion path $L_\mathrm{eff} / 10^{-3}\,\mathrm{m}$, and vapor-in-air diffusion coefficient $D / 10^{-5}\,\mathrm{m^2\,s^{-1}}$ of acetone and HFE-7100 at different temperatures $T/\mathrm{K}$.

| $T$ | $x_v^\circ$ | $N_v^\circ$ | $L_\mathrm{eff}$ | $D$ |
|---|---|---|---|---|
| *Acetone* | | | | |
| 283.15 | 0.1529 | 3.46 | 19.8 | 0.96 |
| 288.15 | 0.1936 | 4.69 | 19.8 | 1.02 |
| 293.15 | 0.2428 | 6.08 | 20.4 | 1.07 |
| 298.15 | 0.3020 | 7.64 | 21.8 | 1.13 |
| 303.15 | 0.3726 | 9.36 | 23.9 | 1.19 |
| 308.15 | 0.4562 | 11.3 | 26.6 | 1.24 |
| 313.15 | 0.5545 | 13.3 | 30.1 | 1.27 |
| *HFE-7100* | | | | |
| 283.15 | 0.1390 | 1.10 | 32.9 | 0.56 |
| 288.15 | 0.1738 | 1.29 | 34.5 | 0.55 |
| 293.15 | 0.2156 | 1.60 | 35.4 | 0.56 |
| 298.15 | 0.2655 | 2.03 | 35.9 | 0.58 |
| 303.15 | 0.3248 | 2.58 | 36.4 | 0.59 |
| 308.15 | 0.3947 | 3.25 | 37.1 | 0.61 |
| 313.15 | 0.4766 | 4.04 | 38.5 | 0.62 |

eters that contribute to the final error, we will consider two, $N_v^\circ$ and $L_\mathrm{eff}$, as they are the main contributors. As stated above, the largest relative error in the evaporation rate $N_v^\circ$ is 7% for HFE-7100 and 12% for acetone. For the effective diffusion length $L_\mathrm{eff}$, the largest relative error is only 1.8% for HFE-7100 and 10% for acetone. We emphasize, that the above errors are the largest among the measurements performed in the temperature range from 283.15 K to 313/15 K. The relative error of $D$ is calculated as the square root of the relative errors

squared of the contributing terms. This evaluation provides the largest relative error for diffusion $D$ which is 7.2% for HFE-7100 and 15.6% for acetone.

The determined diffusion coefficients, together with the error-bars and trend-lines, are shown in Fig. 12, and compared with available literature data. For acetone, the present results agree well within the error bar with the measurements reported in [43, 44, 45, 46] and demonstrate very good agreement with interpolation presented in [8]. For HFE-7100 we presented only our original data.

To parameterize the temperature dependency of the diffusion coefficients, we have fitted them to a kind of the Arrhenius equation

$$D(T) = D_0 \exp\left(-\frac{E_a}{RT}\right) \tag{20}$$

where $D_0$ is a coefficient, and $E_a$ is a so-called activation energy of the process. This fit agrees well with our data, and can be seen as the dashed curves on both panels of Fig. 12.

The numeric values of the fit parameters are:

$D_0 = 2.963 \cdot 10^{-5}\,\mathrm{m^2\,s^{-1}}$ and $E_a = 7055\,\mathrm{J\,mol^{-1}}$ (for acetone),

$D_0 = 1.016 \cdot 10^{-5}\,\mathrm{m^2\,s^{-1}}$ and $E_a = 3882\,\mathrm{J\,mol^{-1}}$ (for HFE-7100).

## 4. Conclusions

In this work, we demonstrate the broad capabilities of optical digital interferometry for measuring the evaporation rate and determining diffusion coefficients, optical contrast coefficients, and temperature drop on the evaporative interface of vapour-air mixtures. The stabilized Mach-Zehnder interferometer with modern phase extraction algorithm allows the tracing of the vapour distribution in the entire two-dimensional cross-section of the cell, both in steady-state and transient regimes. Our findings are based on complete evaporation of a thin liquid layer from a rectangular cuvette with an open end. Evaporation of strongly volatile (acetone) and moderately volatile (HFE-7100) liquids into air was investigated in the temperature range from 283.15 to 313.15 K.
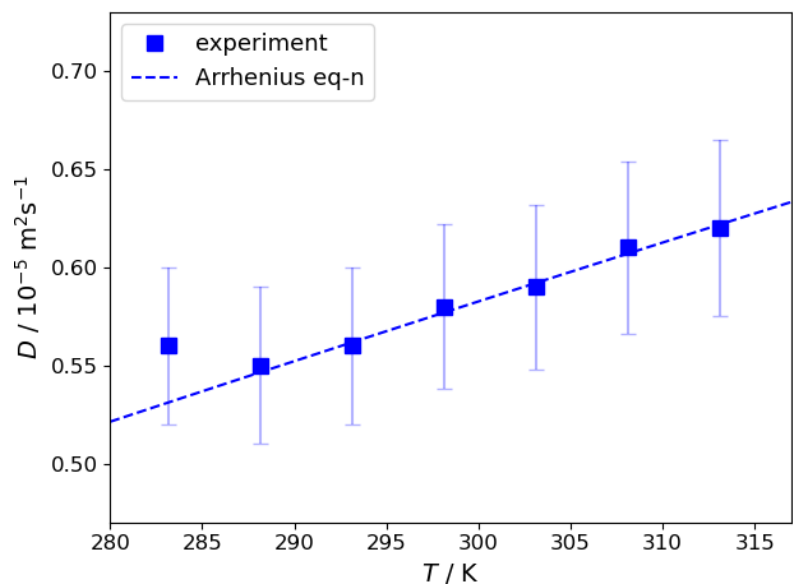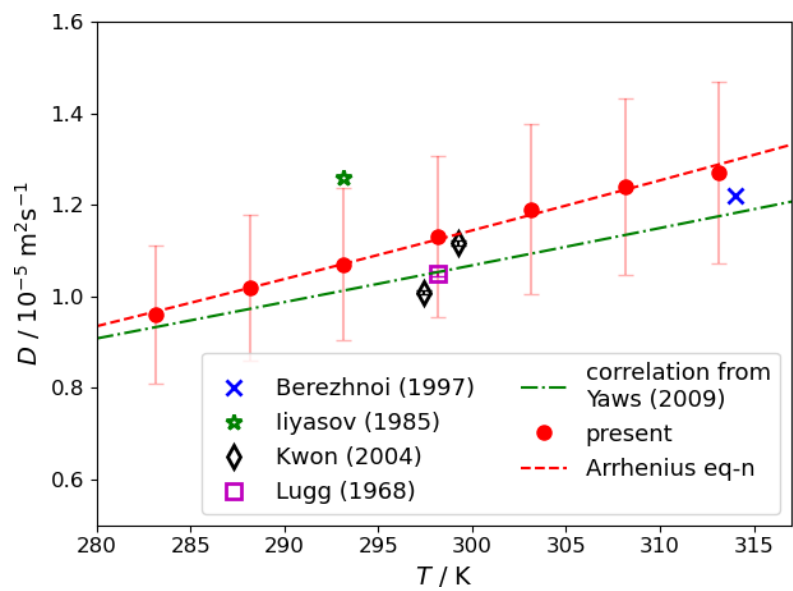
31

Figure 12: Diffusion coefficient of acetone vapor-in-air (top). Comparison of present measurements with literature data at different temperatures. Diffusion coefficient of HFE-7100 vapor-in-air (bottom)

Tracing the evolution of the refractive index, three different temporal regimes of vapour diffusion were identified occurring at different times of the experiment, and among them the longest one corresponds to the steady evaporation. The evaporation rate, as well as the evaporative heat flux, was determined by optical measurements of the evaporation time in the steady regime.

The temperature drop evaluation at the interface revealed that the temperature variation inside the cell is weak enough to neglect its contribution to the refractive index variation, but strong enough to cause Marangoni convection at the interface. The 2D maps of the optical phase clearly showed that the diffusion process was disrupted at both ends of the tube. Near the interface, the Marangoni convection, although weak, remixes vapour and air while near the open end the external air flow partly propagates into the cell volume. Thanks to interferometric 2D images, regions with disturbed diffusion regime were localised and excluded from consideration, so that a true diffusion path was determined in each experiment.

The diffusion coefficients of vapour in air were determined using a working equation based on the "diffusion through a stagnant gas film" model and on the true diffusion path. A good agreement of the measured diffusion coefficients with available literature data for acetone validates the interferometric approach we developed in this work.

The instrument we designed and built, together with the novel experimental procedure we implemented, made it possible to quickly and reliably gain access to important properties of vapour-air mixtures, such as the diffusion coefficient and optical contrast factors in particular. We may therefore conclude that interferometric measurements open new promising perspectives for better control of diffusion of vapour in gases.

## CRediT authorship contribution statement

**V. Shevchenko:** Data Curation, Investigation. **A. Mialdun:** Methodology, Software, Writing - Original Draft. **V. Yasnou:** Investigation, Validation.

Y. V. Lyulin: Formal analysis, Writing - Original Draft H. Ouerdane: Supervision, Writing - Review & Editing. V. Shevtsova: Conceptualization, Supervision, Writing - Review & Editing.

## Declaration of Competing Interest

## Acknowledgments

## References

[1] M. P. Willis, B. A. Mantooth, T. A. Lalain, Novel Methodology for the Estimation of Chemical Warfare Agent Mass Transport Dynamics, Part I: Evaporation, J. Phys. Chem. C 116 (1) (2012) 538–545. `doi:10.1021/jp2087835`.

[2] S. Chapman, T. Cowling, G. D. Burnett, The mathematical theory of non-uniform gases: an account of the kinetic theory of viscosity, thermal conduction and diffusion in gases, Cambridge University Press, 1990.

[3] D. Jafari, A. Franco, S. Filippeschi, P. Di Marco, Two-phase closed thermosyphons: A review of studies and solar applications, Renewable and Sustainable Energy Reviews 53 (2016) 575–593.

[4] L. Zhu, J. Yu, Experimental investigation on startup performances of a separator assisted two-phase loop thermosyphon, International Journal of Heat and Mass Transfer 148 (2020) 119141.

[5] V. Bekezhanova, O. Goncharova, Modeling of three dimensional thermocapillary flows with evaporation at the interface based on the solutions of a special type of the convection equations, Applied Mathematical Modelling 62 (2018) 145–162. `doi:10.1016/j.apm.2018.05.021`.

[6] V. Bekezhanova, O. Goncharova, Problems of evaporative convection (review), Fluid Dynamics 53 (2018) S69–S102. `doi:10.1134/S001546281804016X`.

[7] V. Bekezhanova, O. Goncharova, Numerical study of the evaporative convection regimes in a three-dimensional channel for different types of liquid-phase coolant, International Journal of Thermal Sciences 156 (2020). `doi:10.1016/j.ijthermalsci.2020.106491`.

[8] C. L. Yaws, Chapter 10 - Diffusion Coefficient in Air – Organic Compounds, in: C. L. Yaws (Ed.), Transport Properties of Chemicals and Hydrocarbons, William Andrew Publishing, Boston, 2009, pp. 407–496. `doi:10.1016/B978-0-8155-2039-9.50015-6`.

[9] Y. Lyulin, A. Kreta, H. Ouerdane, O. Kabov, Experimental study of the convective motions by the piv technique within an evaporating liquid layer into the gas flow, Microgravity Science and Technology 32 (2) (2020) 203–216. `doi:10.1007/s12217-019-09759-x`.

[10] D. Zaitsev, A. Semenov, O. Kabov, Effect of viscosity on thermocapillary breakdown of a falling liquid film, Thermophysics and Aeromechanics 23 (4) (2016) 625–628. `doi:10.1134/S0869864316040168`.

[11] D. Zaitsev, D. Kirichenko, V. Ajaev, O. Kabov, Levitation and self-organization of liquid microdroplets over dry heated substrates, Physical Review Letters 119 (9) (2017). `doi:10.1103/PhysRevLett.119.094503`.

[12] H. Y. Erbil, Evaporation of pure liquid sessile and spherical suspended drops: A review, Advances in Colloid and Interface Science 170 (1) (2012) 67–86. `doi:10.1016/j.cis.2011.12.006`.

[13] N. M. Kovalchuk, A. Trybala, V. M. Starov, Evaporation of sessile droplets, Current Opinion in Colloid & Interface Science 19 (4) (2014) 336–342. `doi:10.1016/j.cocis.2014.07.005`.

[14] S. Somasundaram, T. N. C. Anand, S. Bakshi, Evaporation-induced flow around a pendant droplet and its influence on evaporation, Physics of Fluids 27 (11) (2015) 112105. `doi:10.1063/1.4935355`.

[15] D. Melnikov, T. Takakusagi, V. Shevtsova, Enhancement of evaporation in presence of induced thermocapillary convection in a non-isothermal liquid bridge, Microgravity Science and Technology 25 (1) (2013) 1–8. `doi:10.1007/s12217-012-9319-4`.

[16] H. Machrafi, Y. Lyulin, C. Iorio, O. Kabov, P. Dauby, Numerical parametric study of the evaporation rate of a liquid under a shear gas flow: Experimental validation and the importance of confinement on the convection cells and the evaporation rate, International Journal of Heat and Fluid Flow 72 (2018) 8–19, cited By 2. `doi:10.1016/j.ijheatfluidflow.2018.05.003`.

[17] Y. Lyulin, O. Kabov, Evaporative convection in a horizontal liquid layer under shear-stress gas flow, International Journal of Heat and Mass Transfer 70 (2014) 599–609. `doi:10.1016/j.ijheatmasstransfer.2013.11.039`.

[18] A. Charogiannis, F. Beyrau, Laser induced phosphorescence imaging for the investigation of evaporating liquid flows this article is part of the topical collection on application of laser techniques to fluid mechanics 2012, Experiments in Fluids 54 (5) (2013). `doi:10.1007/s00348-013-1518-2`.

[19] P. L. Kelly-Zion, C. J. Pursell, N. Hasbamrer, B. Cardozo, K. Gaughan, K. Nickels, Vapor distribution above an evaporating sessile drop, Int. J. Heat Mass Tran. 65 (2013) 165–172. `doi:10.1016/j.ijheatmasstransfer.2013.06.003`.

[20] A. K. Grob, M. M. El-Wakil, An Interferometric Technique for Measuring

36

Binary Diffusion Coefficients, J. Heat Transfer 91 (2) (1969) 259–265. `doi:10.1115/1.3580138`.

[21] W. Z. Black, R. L. Somers, Interferometric method for the determination of binary gas mass diffusivities, Rev. Sci. Instrum. 48 (4) (1977) 476–481. `doi:10.1063/1.1135054`.

[22] S. Dehaeck, A. Rednikov, P. Colinet, Vapor-Based Interferometric Measurement of Local Evaporation Rate and Interfacial Temperature of Evaporating Droplets, Langmuir 30 (8) (2014) 2002–2008. `doi:10.1021/la404999z`.

[23] A. Mialdun, I. Ryzhkov, O. Khlybov, T. Lyubimova, V. Shevtsova, Measurement of soret coefficients in a ternary mixture of toluene-methanol-cyclohexane in convection-free environment, J. Chem. Phys. 148 (4) (2018) 044506.

[24] E. Lapeira, A. Mialdun, V. Yasnou, P. Aristimuño, V. Shevtsova, M. Bou-Ali, Digital interferometry applied to thermogravitational technique., Microgravity Sci. Tech. 30 (2018) 635–641.

[25] A. Mialdun, V. Shevtsova, Temperature dependence of Soret and diffusion coefficients for toluene-cyclohexane mixture measured in convection-free environment, J. Chem. Phys. 143 (22) (2015) 224902.

[26] T. R. Marrero, E. A. Mason, Gaseous Diffusion Coefficients, J. Phys. Chem. Ref. Data 1 (1) (1972) 3–118. `doi:10.1063/1.3253094`.

[27] J. M. Pommersheim, J. T. Seeley, J. van Kirk, Use of the Stefan cell to obtain solvent diffusivities, The Chemical Engineering Journal 23 (1) (1982) 105–109. `doi:10.1016/0300-9467(82)85013-2`.

[28] A. N. Berezhnoi, P. A. Norden, Diffusion length in a stefan cell, Journal of Engineering Physics 59 (5) (1990) 1448–1450. `doi:10.1007/BF00872965`.

[29] A. Parker, R. Babas, Thermogravimetric measurement of evaporation: Data analysis based on the Stefan tube, Thermochimica Acta 595 (2014) 67–73. `doi:10.1016/j.tca.2014.09.011`.

[30] M. E. Graniela, C. A. Ramírez, Effect of a sweeping air stream and gas–phase aspect ratio of an isothermal Stefan diffusion column on the experimental estimation of binary gas diffusivities, Chemical Engineering Communications 206 (7) (2019) 842–860. `doi:10.1080/00986445.2018.` `1530992`.

[31] J. Coca, J. L. Bueno, R. Alvarez, Gaseous Diffusion Coefficients by the Stefan-Winkelmann Method Using a Polymer-Solvent Mixture as Evaporation Source, Ind. Eng. Chem. Fund. 19 (2) (1980) 219–221. `doi:` `10.1021/i160074a016`.

[32] M. d. S. Jaime, S. G. Maisonet, C. A. Ramírez, Effect of liquid phase composition on the experimental determination of binary gas diffusivities in an isothermal Stefan diffusion column, Chemical Engineering Communications 0 (0) (2019) 1–27. `doi:10.1080/00986445.2019.1674815`.

[33] C. Y. Lee, C. R. Wilke, Measurements of Vapor Diffusion Coefficient, Ind. Eng. Chem. 46 (11) (1954) 2381–2387. `doi:10.1021/ie50539a046`.

[34] K. J. Beverley, J. H. Clint, P. D. I. Fletcher, Evaporation rates of pure liquids measured using a gravimetric technique, Phys. Chem. Chem. Phys. 1 (1) (1999) 149–153. `doi:10.1039/A805344H`.

[35] A. Mialdun, V. Shevtsova, Development of optical digital interferometry technique for measurement of thermodiffusion coefficients, Int. J. Heat Mass Trans. 51 (11) (2008) 3164–3178.

[36] A. Mialdun, V. Shevtsova, Measurement of the Soret and diffusion coefficients for benchmark binary mixtures by means of digital interferometry, J. Chem. Phys. 134 (4) (2011) 044524. `doi:10.1063/1.3546036`.

[37] V. Majer, V. Svoboda, Enthalpies of vaporization of organic compounds : a critical review and data compilation, 1st Edition, Vol. 32 of IUPAC Chemical Data, Blackwell Scientific Publications, Oxford, 1985.

[38] 3M, St. Paul, MN, USA, 3M™Novec™7100 Engineered Fluid (Sep. 2009).
URL https://multimedia.3m.com/mws/media/1998180/
3m-novec-7100-engineered-fluid.pdf

[39] D. Ambrose, C. H. S. Sprake, R. Townsend, Thermodynamic properties of organic oxygen compounds XXXIII. The vapour pressure of acetone, J. Chem. Thermodyn. 6 (7) (1974) 693–700. doi:10.1016/0021-9614(74)90119-0.

[40] J. Van Vleck, The theory of electric and magnetic susceptibilities, International series of monographs on physics, University press, 1932.

[41] M. Gebhardt, W. Köhler, A. Mialdun, V. Yasnou, V. Shevtsova, Diffusion, thermal diffusion, and Soret coefficients and optical contrast factors of the binary mixtures of dodecane, isobutylbenzene, and 1,2,3,4-tetrahydronaphthalene, J. Chem. Phys. 138 (11) (2013) 114503. doi:10.1063/1.4795432.

[42] R. B. Bird, W. E. Stewart, E. N. Lightfoot, D. J. Klingenberg, Introductory Transport Phenomena, Wiley, 2014.

[43] G. A. Lugg, Diffusion coefficients of some organic and other vapors in air, Anal. Chem. 40 (7) (1968) 1072–1077. doi:10.1021/ac60263a006.

[44] L. V. Iiyasov, Y. B. Negrtov, Zavod. Lab. 51 (1985) 32–34.

[45] A. N. Berezhnoi, A. V. Semenov, Binary Diffusion Coefficients of Liquid Vapors in Gases, Begell House, 1997.

[46] K. C. Kwon, T. H. Ibrahim, Y. Park, C. M. Simmons, Pseudo-binary molecular diffusion of vapors into air, Advances in Environmental Research 8 (3) (2004) 667–678. doi:10.1016/S1093-0191(03)00039-X.